A star-test wavefront sensor using neural network analysis

Baudat, Gaston, Hayes, John

Gaston Baudat, John B. Hayes, "A star-test wavefront sensor using neural network analysis," Proc. SPIE 11490, Interferometry XX, 114900U (21 August 2020); doi: 10.1117/12.2568018

SPIE.

Event: SPIE Optical Engineering + Applications, 2020, Online Only

A Star-Test Wavefront Sensor Using Neural Network Analysis

Gaston Baudat[1] and John B. Hayes[2]

[1]Innovations Foresight, LLC., 24 Ramblewood Drive, Glenmoore, PA. 19343, USA

[2]Adjunct Research Professor, Wyant College of Optical Sciences, The University of Arizona, 1630 E. University Blvd., Tucson, Arizona 85721, USA

Abstract: We describe a new, simple wavefront sensing method that uses a single measurement of a defocused star and a neural network to determine low-order wavefront components. The neural net is trained on computed diffracted star image data at 640 nm to output annular Zernike terms for an obscured circular aperture over a discrete range of all values. In the context of an actual star, the neural-net also provides the Fried's parameter as an estimation of atmospheric turbulence. It is shown that the neural-net can produce a robust, high accuracy solution of the wavefront based on a single measurement. The method can also be used to simultaneously determine both on-axis and field-dependent wavefront performance from a single measurement of stars throughout the field. The prototype system can run at a rate of about 1 Hz with Python interpreted code, but higher speeds, up to video rates, are possible with compilation, proper hardware and optimization. This technique is particularly useful for low-order active-optics control and for optical alignment. A key advantage of this new method is that it only requires a single camera making it a simple cost-effective solution that can take advantage of an existing camera that may already be in an optical system. Results for this method are compared to high-precision interferometric data taken with a 4D Technology, PhaseCam interferometer and with an Innovations Foresight StarWave Shack Hartmann sensor from ALCOR SYSTEM under well-controlled conditions to validate performance. We also look at how the system has been implemented to use starlight for aligning multiple mirror telescopes in the presence of atmospheric seeing.

1. INTRODUCTION

Astronomers have used defocused star images to perform telescope alignment and to estimate optical performance for a long time [1]. The classical star test adds a defocus bias to the test wavefront, which defines the amount of aberration that can be detected without ambiguity. The minimum defocus required is function of the amplitude of higher order aberrations. The defocus bias determines the sign of defocus and also limits the amount of defocus relative to the bias term that can be accurately estimated. The method is related to curvature wavefront sensing and relies on the fact that if the total aberration is smaller than the defocus bias, the resulting diffraction pattern displayed in the defocused PSF image is unique for any arbitrary combination of aberration components in the wavefront. Methods for visually estimating the optical performance of telescopes using star testing have been formalized [2] and methods to use digital imaging of star images to more accurately reconstruct wavefront data have been ongoing.

Roddier and Roddier [3] developed an iterative method of estimating the wavefront in the pupil from differential star image data taken nearly simultaneously on either side of the best focus position in order to cancel out scintillation. This approach can reconstruct the full wavefront but the results are sensitive to factors such as noise and the initial input conditions and it requires a configuration that allows near-simultaneous data collection. Furthermore, solving the irradiance transport equation using iterative numerical techniques is prone to local minima and convergence issues, especially when the aberrations are large. In spite of these difficulties, this approach has been used successfully for astronomical adaptive and active optical systems.

Hickson [4,5] shows that under some conditions, a single defocused image of a point source contains enough information to uniquely determine the phase of an incident wavefront. Hickson demonstrates

Interferometry XX, edited by Michael B. North Morris, Katherine Creath, Rosario Porras-Aguilar, Proc. of SPIE Vol. 11490, 114900U· © 2020
SPIE · CCC code: 0277-786X/20/$21 · doi: 10.1117/12.2568018

analyzing curvature components of the intensity distribution across a defocused spot allows retrieval of wavefront curvature, tilt, and spherical aberration. A key difficulty of these approaches is that there is no closed form solution for working backwards from the defocused image to the initial wavefront.

Yobei, et al. [6] introduced the use of deep learning to wavefront sensing methods to address these limitations. They used a spatial light modulator to create learning data from an actual physical system for neural network (NN) training but did not solve the problem for general data analysis--and as the authors pointed out, "It is also important to compare the DLWFS [deep learning wavefront system] with conventional wavefront sensors to validate its usefulness as a practical replacement."

A key advantage of the AI approach over curvature wavefront sensing methods [3] is that it provides a direct solution of the Zernike coefficients or Seidel wavefront coefficients, including the defocus term, using a direct feedforward neural network. Therefore, after training, there are no iteration or convergence considerations when solving for the wavefront. In our work, the NN was trained to learn an inverse function, typically the Zernike coefficients, or any other relevant figure of merit, starting from the defocused point spread function (PSF) computed from diffraction theory. Once trained, the AI system can be used directly on many other applications without retraining. In its simplest form, the AI hardware is just a camera taking defocused images of a single point source. However, with the appropriate synthetic data, many types of source and optical layouts can be considered, such multi-point sources for simultaneously evaluating both on and off-axis wavefront performance, as well as extended sources when required.

It is important to understand that neural networks do not necessarily converge to a perfect analytic solution even in a context of a well-posed problem; instead, the network is "trained" to produce "a likely result", which raises questions about the ultimate repeatability and accuracy of the output as well as about the factors that might affect the output. Therefore, a key motivation of this work is to explore how well this approach agrees with other, more well-established metrology methods such as digital interferometry and Shack Hartmann wavefront sensors. We also explore some of the factors that affect the accuracy and precision of the results. Finally, we will take a look at how the system can be implemented to work in the presence of atmospheric seeing using an actual star.

2. METHODOLOGY

The far field, intensity distribution of the monochromatic point spread function (PSF) is given by the square modulus of the two-dimensional Fourier transform of the complex pupil function:

$$PSF(u,v) = |\mathcal{FF}\{(t(x,y)\}|^2. \quad [1]$$

The complex pupil function (t(x,y)) contains information about the shape of the pupil, the transmission function and optical phase in the pupil. In general, the complex pupil function is defined as follows:

$$t(x,y) = t_0(x,y)e^{i\varphi(x,y)} \quad [2]$$

where: $t_0(x,y)$ = pupil amplitude transmission function,
$\varphi(x,y)$ = the pupil phase function = $2\pi W(x,y)/\lambda$, and
$W(x,y)$ = wavefront departure from the reference sphere.

With the required scaling factors, the PSF for an axially symmetric system becomes:

$$PSF(r') = \frac{I_0}{(\lambda f)^2}|T(\rho)|^2_{\rho=r'/\lambda f} \quad [3]$$

Where:

I_0 = the irradiance in power/area incident on the pupil,

λ = operating wavelength,
f = focal length,
r'= radial coordinate in the focal plane,
T(ρ) = $\mathcal{F}\{t(r)\}$ = Radial Fourier transform (Hankel transform) of the complex pupil function.

For a circular, unobscured aperture, the amplitude transmission function (t_0) is given by the cylinder function, which is defined as:

$$cyl(r) = \begin{cases} 1, & 0 \le r < 1/2 \\ \frac{1}{2}, & r = 1/2 \\ 0, & r > 1/2 \end{cases} \quad [4]$$

Using equation [3], it is straightforward to numerically compute the monochromatic PSF for any phase distribution in the pupil. Baudat [7] has shown how the input data can be normalized and sampled for general application to any optical system.

In practical terms, it is useful to use the radial annular Zernike polynomials to construct a limited set of aberrations most appropriate for the application. For example, this approach is particularly useful for aligning many types of two-mirror telescope systems where minimizing on-axis coma insures optimum secondary mirror alignment and minimizing spherical optimizes mirror spacing. It is also useful to be able to identify astigmatic and trefoil terms to optimize field performance and to identify potential mechanical mounting stress. For this purpose, it is sufficient to train the NN to identify only the 9 Zernike terms shown in Table 1. Obviously, this is not a limitation of the method, which could be trained to identify higher order terms and atmospheric seeing parameters. The only limitation relates to the size of the neural-net database and the amount of time required for computing the input data and training the system.

Name	**Index**	**Radial Annular Polynomials** $0 < r \le 1 \quad 0 < \epsilon \le 1 \quad 0 \le \theta \le 2\pi$
Defocus	Z_3	$(2r^2 - 1 - \varepsilon^2)/(1 - \varepsilon^2)$
Vertical astigmatism	Z_4	$\left(r^2/\sqrt{1+\epsilon^2+\epsilon^4}\right) cos(2\theta)$
Oblique astigmatism	Z_5	$\left(r^2/\sqrt{1+\epsilon^2+\epsilon^4}\right) sin(2\theta)$
Horizontal coma	Z_6	$[3r^3(1+\epsilon^2) - 2r(1+\epsilon^2+\epsilon^4)]/\left[(1-\epsilon^2)\sqrt{(1+\epsilon^2)(1+4\epsilon^2+\epsilon^4)}\right] cos(\theta)$
Vertical coma	Z_7	$[3r^3(1+\epsilon^2) - 2r(1+\epsilon^2+\epsilon^4)]/\left[(1-\epsilon^2)\sqrt{(1+\epsilon^2)(1+4\epsilon^2+\epsilon^4)}\right] sin(\theta)$
Primary spherical	Z_8	$(6r^4 - 6r^2(1+\epsilon^2) + 1 + 4\epsilon^2 + \epsilon^4)/(1-\epsilon^2)^2$
Oblique trefoil	Z_9	$\left[r^3/\sqrt{1+\epsilon^2+\epsilon^4+\epsilon^6}\right] cos(3\theta)$
Vertical trefoil	Z_{10}	$\left[r^3/\sqrt{1+\epsilon^2+\epsilon^4+\epsilon^6}\right] sin(3\theta)$
Secondary spherical	Z_{15}	$[(20r^6 - 30r^4(1+\epsilon^2) + 12r^2(1+3\epsilon^2+\epsilon^4) - (1+9\epsilon^2+9\epsilon^4+\epsilon^6)]/(1-\epsilon^2)^3$

Table 1 Definition of the nine radial annular Zernike terms using the Wyant-Creath [8] numbering convention, following Mahajan's [9] definitions. These are the terms used for generating synthetic data and for training the AI system described here with $\varepsilon = 0$ for the optical bench experiments.

A limit of +/-0.25 rms waves was placed on each Zernike term and even with just 9 terms, the number of images that has to be computed can become quite large if a uniform variation of each value were required across the range. For example, if the desired step size is set at 0.005 waves, each term would generate 100 sample values and the database would require 10^{10} entries. Fortunately, a NN does not require uniformly spaced sampling to produce a high-resolution result since the function to be learned is smooth and continuous by nature. Instead, the database is simply filled with randomized values across the range of possibilities for each Zernike term using a total of 300,000 to 600,00 entries. The time needed to compute the data and train the NN is on the order of 20+ hours. However, once trained, the neural net runs at a rate of about 1 Hz on a mid-level Windows PC running Python interpreted code. Video rates, are possible with compilation, dedicated hardware and optimization. Figure 1 shows the basic steps used to load and train the neural network.

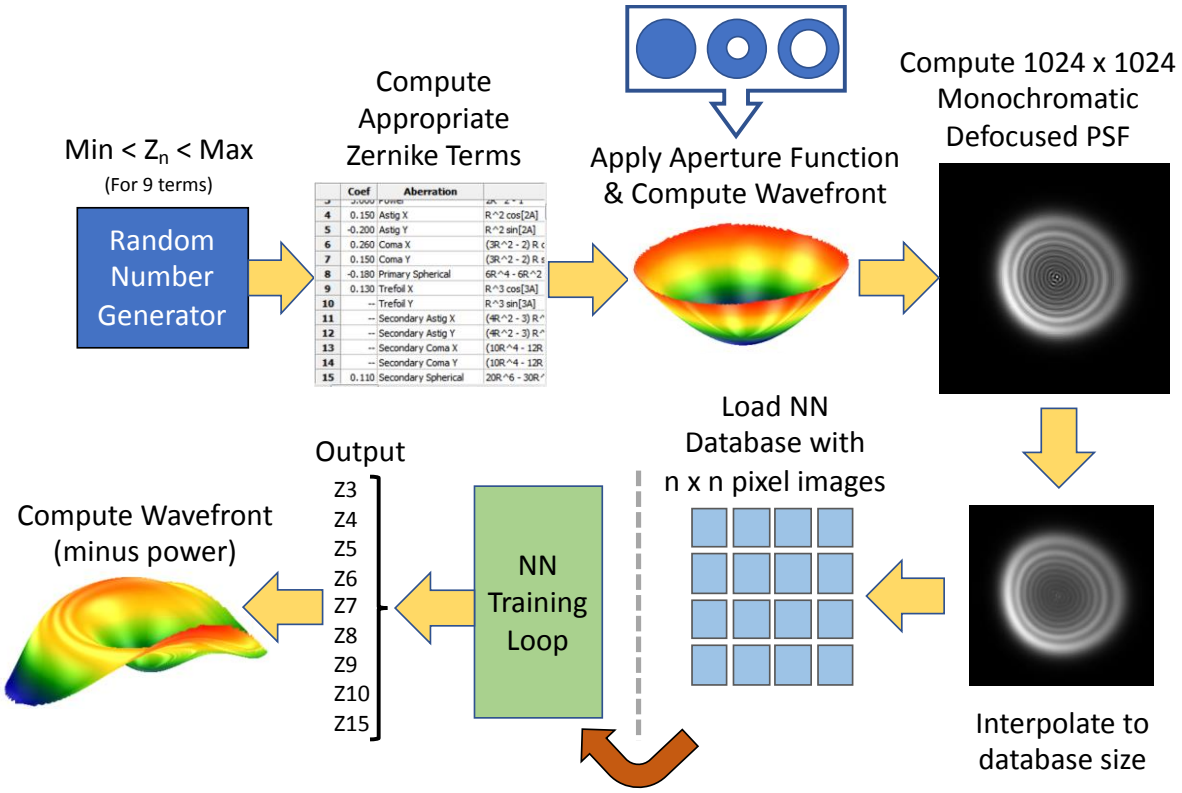

Figure 1. The basic steps for loading data and training the neural network (NN) to recognize 9 Zernike terms. The training data can also include atmospheric parameters and for the effects of non-point sources.

3. OUTPUT VALIDATION AND DISPERSION

Once the AI system is trained, a second independent set of defocused spots computed from randomized Zernikes were generated to test the output dispersion for each term. Table 2 compares the results for 25,000 randomized test cases using 256 x 256 pixel images and 128 x 128 pixel images. The data shows that training the NN with 256 x 256 pixel images produces an output with an average uncertainty of about +/- 10 milli-waves. With 128 x 128 pixel data, the uncertainty increases by about 30% to +/- 13 milli-waves. For many applications that require higher computational speed, less memory and may not be impacted by slightly greater uncertainty, using a smaller data set may be a

viable option. Given the small irradiance differences between spot images separated by only 0.01 waves, the AI solution demonstrates remarkable sensitivity to small changes in the test data.

Term	Zernike	256x256	128x128
Defocus	Z3	9.0	10.0
Spherical	Z8	9.0	9.0
Astig X	Z4	12.0	15.0
Astig Y	Z5	7.0	20.0
Coma X	Z6	11.0	17.0
Coma Y	Z7	11.0	11.0
Trefoil X	Z9	11.0	17.0
Trefoil Y	Z10	14.0	11.0
Secondary Spherical	Z15	8.0	8.0
Average		**10.2**	**13.1**
Median		**11.0**	**11.0**

Table 2 AI output dispersion expressed as the rms variation in output over 25,000 test cases for 9 individual Zernike terms with 256x256 and 12x128 pixel data sets in units of milliwaves (mw). The uncertainty of the magnitude of the astigmatic, comatic, and trefoil terms will simply be given by the quadrature sum of x,y components.

4. COMPARISON TO INTERFEROMETRY

The important question is: How well does the AI result compare to other methods? In order to compare measurements from different techniques, the simple test bench shown in figure 2 was used to measure a simple cemented achromat in double pass. The source is a white light LED with a diffuser to help completely illuminate the full F/12.5 exit pupil through a 10-micron pinhole. Light from the pinhole is reflected from a high quality, 2-micron thick, 50:50 pellicle beam splitter to a cemented achromat (Edmund 25 mm diameter x 300 mm FL, mounted with a 24 mm clear aperture.). The spacing is adjusted to collimate the output so that it can be reflected in double-pass back through the lens and focused on a 16 Mpx, ZWO ASI1600MM CMOS monochrome camera. By slightly defocusing the spot a fixed amount, data from the camera feeds the AI network, which outputs 9 Zernike terms. A 3-mm thick broadband red filter is positioned in front of the camera to limit the spectral bandwidth.

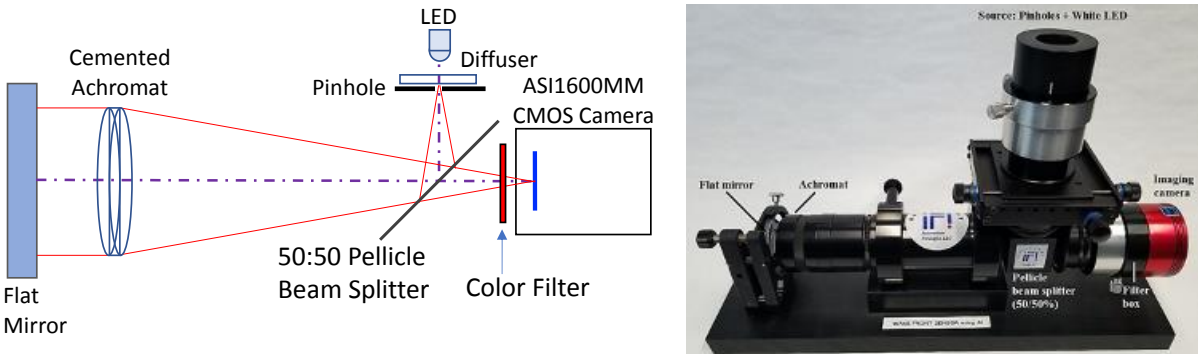

Figure 2. The test bench used to measure the wavefront. The color filters used in this work are 3 mm thick and introduce 0.6 milliwaves of spherical aberration on-axis at F/12.5 so the impact on the results is negligible. The 50:50 pellicle beam splitter is 2 microns thick, which may introduce a minor anamorphic error into the reflected illuminating beam. Its effect on the transmitted beam will be negligible.

It should be noted that while the 25.4 mm pellicle beam splitter is nominally flat, the flatness specification for these type of beam splitters is typically in the range of 0.5–1.0 waves over the full aperture. In this case, less than about 2.5 mm of the full aperture is illuminated by the F/12.5 test beam, which may still introduce a small anamorphic error into the test wavefront. There was no attempt to fully characterize this particular limitation because it should have a relatively minor effect on the results. Furthermore, any errors introduced in the transmitted beam should be negligible for our purposes here.

By simply removing the ZWO camera from the test bench, an interferometer or a Shack-Hartmann sensor could be used to measure the same wavefront to allow direct comparison between measurement methods. The interferometer used was a 4D Technology model 6000 PhaseCam [ref 10-13] with a F/10 diverger lens. The PhaseCam is a polarization Twyman-Green type interferometer with a fiber-fed, single-mode stabilized HeNe laser source. It makes single-fame phase measurements with exposures as short as 20 micro-seconds, which makes it very insensitive to mechanical vibration and allows wavefront averaging to reduce uncertainty due to uncorrelated random errors such as those introduced by air turbulence [ref 14].

Measurements were made of both the basic, on-axis wavefront and of the wavefront created by mechanically distorting the return mirror. Some uncertainty in the angular orientation of the data was introduced by removing and replacing the ZWO camera but we have attempted to minimize that effect to less than 5 degrees in the data presented here.

The PhaseCam was configured to average 32 phase individual measurements to time average small statistically random errors that may be introduced by air turbulence. The small air path, a cloth shroud, and signal averaging reduced the uncertainty in the measurement due to air turbulence to less than +/- 0.005 waves. The AI measurements were made using 2-second exposures to time average any residual turbulence in the system. Finally, the absolute accuracy of the PhaseCam data was checked against a fast calibration test sphere. Figure 3 shows that uncalibrated absolute accuracy of the PhaseCam was better than about +/- 0.01 waves over the F/12.5 beam using the 9 Zernike terms of interest.

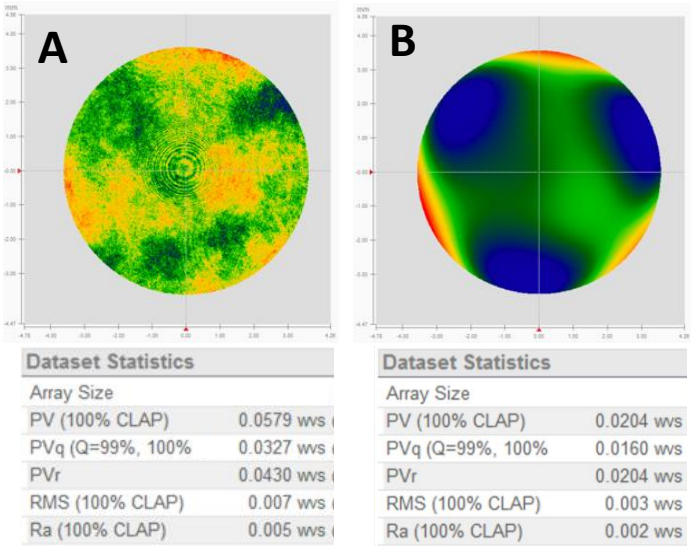

Figure 3. PhaseCam measurements of a 1/20 wave, certified calibration sphere over f/12.5. A) Raw wavefront data, B) The wavefront derived from the 9 Zernike terms used by the AI system.

Figures 4 and 5 show the results for the two methods for measurements of the system with the return mirror mechanically distorted and relaxed to its nominally flat surface. The PV and rms values are quite close but there is noticeable disagreement in both the third order coma and spherical aberration terms. For the relaxed flat mirror the third order coma is 45mw larger with the AI method, while 3rd order spherical is 91mw larger with the opposite sign from the AI data, which is pretty much the same absolute difference as in the measurements of the warped mirror. From those two parameters, there appeared to be a clear systematic difference between interferometry and the AI results.

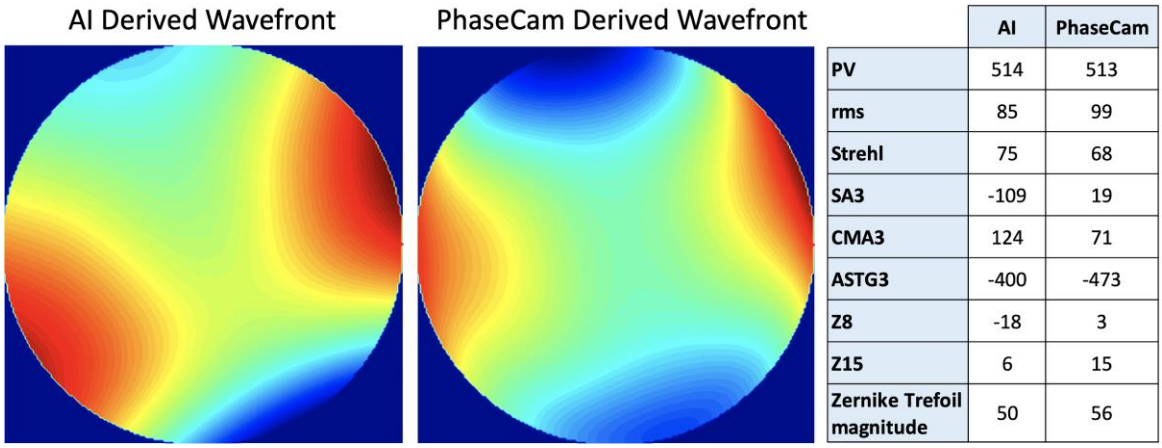

	AI	PhaseCam
PV	514	513
rms	85	99
Strehl	75	68
SA3	-109	19
CMA3	124	71
ASTG3	-400	-473
Z8	-18	3
Z15	6	15
Zernike Trefoil magnitude	50	56

Figure 4. Comparison of initial results (in milliwaves) of a mechanically **distorted** mirror with 10-micron pinhole and broadband red filter AI source. PhaseCam data taken at 633 nm. These contour plots were derived from the measured Zernike coefficients and scaled with the same colors for direct comparison. SA3, CMA3, and ASTG3 are the primary 3rd order Seidel aberrations.

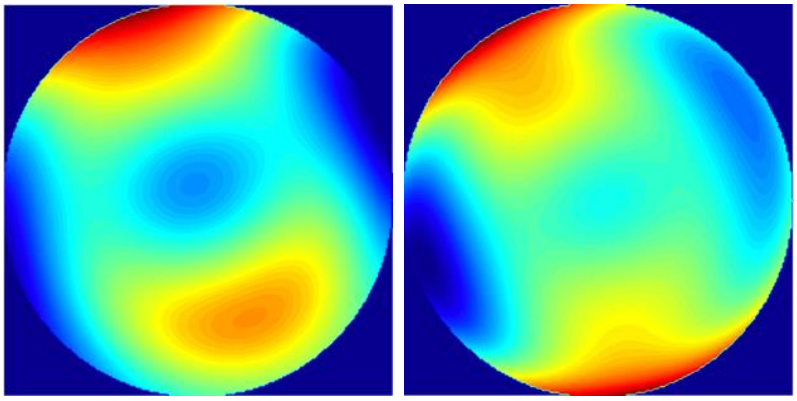

	AI	PhaseCam
PV	139	135
rms	24	22
Strehl	98	98
SA3	-102	11
CMA3	61	16
ASTG3	101	-102
Z8	-17	2
Z15	8	12
Zernike Trefoil magnitude	50	18

Figure 5. Comparison of initial results (in milliwaves) of **relaxed, flat** mirror with 10-micron pinhole and broadband red filter for the AI source. PhaseCam data taken at 633 nm. These contour plots were derived from Zernike data and scaled with the same colors for direct comparison. SA3, CMA3, and ASTG3 are the primary 3rd order Seidel aberrations.

To get at the cause for this discrepancy, we have to remember that there are two fundamental differences between the PhaseCam and AI measurements. First, the PhaseCam uses a monochromatic laser for a direct measurement of the wavefront, while AI was done with a red broadband source

centered at 640nm with a bandwidth of 120nm. Second, the AI system used a 10-micron pinhole that is incoherently illuminated even though the synthetic training data was computed for a monochromatic point source. Therefore, we suspected that the differences are due to the polychromatic and extended nature of the source. Indeed, we found that by simply replacing the 10 microns pinhole with a 5 microns pinhole using the same red filter on-axis leads to an immediate reduction in the measured value of SA3 by a factor of about two.

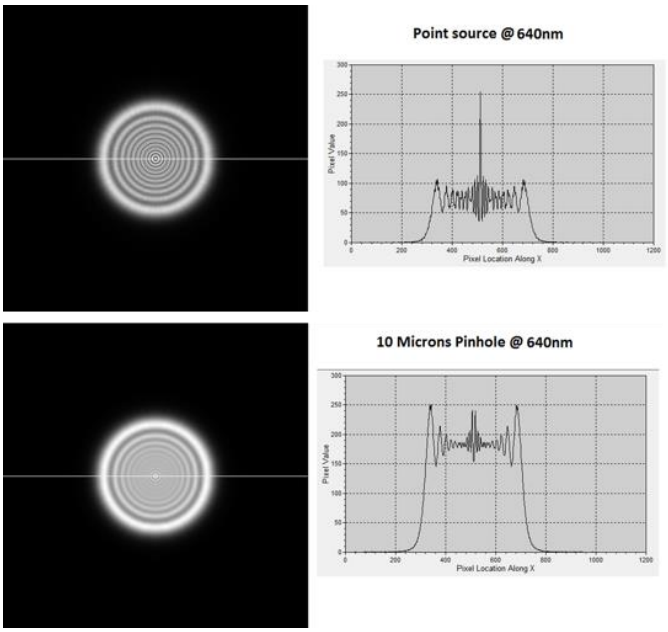

Figure 6. Computed defocused PSFs (3 waves rms = 10.4 waves pv, 1024 x 1024 pixels) @640nm of diffraction limited (no aberration) using a point source (top image) and a 10 microns pinhole with simulated incoherent illumination (bottom image). The bottom spot was computed by incoherently summing the pattern from one point source at the center and 8 equally spaced point sources around the edge of a 10-micron pinhole. The AI system is easily able to detect this level of difference between the spots, which can introduce errors into the output.

To confirm this idea, we generated a new NN data set assuming an incoherently illuminated 10-micron pinhole. An incoherent model was then created by simply incoherently summing the point response over a central point and at 8 equally spaced points around the circumference of the 10-micron pinhole. Figure 6 shows a simulation of a monochromatic sources at 640nm with a point source compared to a 10-micron incoherently illuminated pinhole. We can clearly see the impact on the irradiance distribution by using an incoherent 10-micron pinhole--even though it is only about *half* the 19.5-micron diameter of the Airy disk at F/12.5.

Figure 7 shows the results of new measurements, on axis with a relaxed mirror, from an AI system trained to use a 10-micron incoherent pinhole and a physical 7nm Hα narrowband filter centered at 656 nm in front of the camera. Clearly, this improves the agreement for the spherical aberration terms and brings it to within the uncertainty between the two measurements, which is in the range of +/- 15 milliwaves. These particular measurements were made independently under different conditions so it's difficult to definitively sort out the remaining minor disagreement in field terms due to small difference in the field angles. Clearly, the sensitivity of the AI system is high enough to warrant care in accurately computing the training database to take into account the expected measurement conditions along with the accuracy requirements.

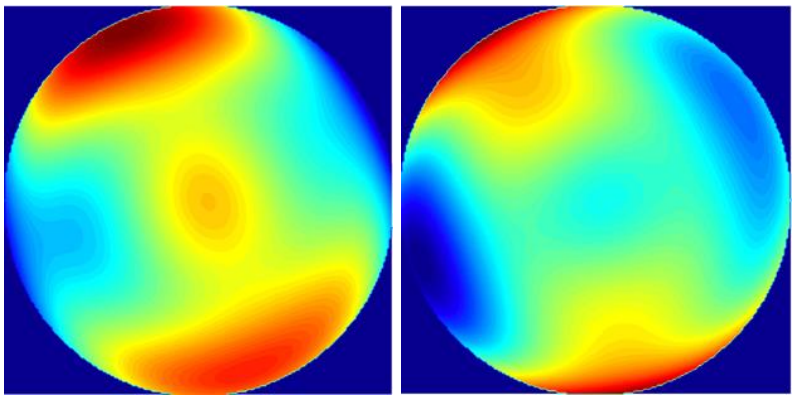

	AI	PhaseCam
PV	166	135
rms	27	22
Strehl	97	98
SA3	18	11
CMA3	36	16
ASTG3	-127	-102
Z8	3	2
Z15	-16	12
Zernike Trefoil magnitude	14	18

Figure 7. Comparison of initial relaxed mirror measurements (in milliwaves) using 10-micron pinhole and a narrowband red filter at 656 nm (7 nm bandpass) in front of the camera with simulated 10-micron database and PhaseCam data taken at 633 nm. These contour plots were derived from Zernike data and scaled with the same colors for direct comparison. SA3, CMA3, and ASTG3 are the primary 3rd order Seidel aberrations. These data sets were not taken concurrently so there may be additional small errors relative to the original measurements; however, there is clearly better agreement in the measured value of SA3 and the Z8 and Z15 terms.

5. COMPARISON TO SHACK HARTMANN

Finally, AI measurements of the test bench were compared to a Shack-Hartmann sensor with a 40x40 lenslet array from Innovations Foresight and manufactured by ALCOR SYSTEM. Unfortunately, the position of the defocused spot on the SH camera is offset from the ZWO camera center used as a reference for the PhaseCam data by about one millimeter or so, we cannot directly compare the PhaseCam and SH data sets. However, since SH and AI were in the same position, and since they both measure the pinhole source through the same optical path, we can directly compare the SH and AI data. The results shown in Figure 8 demonstrate very good agreement.

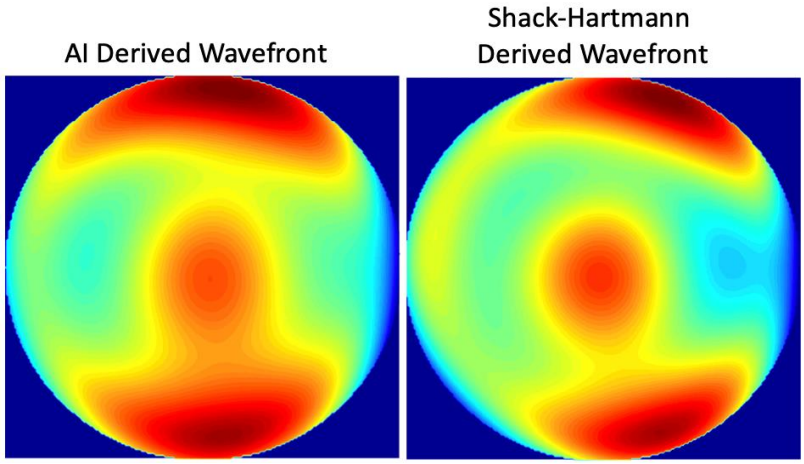

	AI	SH
PV	95	84
rms	15	14
Strehl	99	99
SA3	12	30
CMA3	32	30
ASTG3	-68	-52
Z8	2	5
Z15	-13	-17
Zernike Trefoil magnitude	8	21

Figure 8. Comparison of on-axis measurements (in milliwaves) with the relaxed return mirror using the 10-micron pinhole and narrowband red filter at 656 nm (7 nm bandpass) using the simulated 10-micron database and Innovations Foresight 40x40 lenslet Shack-Hartman sensor measurement using the same source and light path.

6. USING STELLAR SOURCES

A key application that motivated this work is the alignment of multi-mirror telescopes using stars as a source. This application includes two additional considerations over the laboratory measurements presented here. First, the AI system must be trained to handle an obscured aperture and depending on the optical configuration, that may include training for additional structures in the pupil such as spider vanes. None of that is particularly difficult but as we've shown here, the accuracy of the output is dependent on the fidelity of the input.

The second consideration is atmospheric seeing, which ultimately limits the output accuracy that can be achieved. Kolmogorov's turbulence theory [15] provides the relationship between Fried's atmospheric coherence parameter r_0 and the stellar FWHM in radians, known as β, of the seeing limited star image.

$$\beta \cong 0.98\ \lambda/r_0 \qquad [5]$$

The long-exposure stellar profile is most accurately expressed using a Moffat function [16], however for most practical purposes, a Gaussian function will provide acceptable results for computing defocused star images and it is particularly easy implement. Using equation [5], the seeing induced Gaussian kernel width σ, in radians, is given by:

$$\sigma = \frac{\beta}{2\sqrt{2\ln(2)}} \cong 0.42\ \frac{\lambda}{r_0} \qquad [6]$$

Under the sky, data can be taken using exposures ranging from 0.1 to 100 seconds to produce a time averaged PSF that can be matched by the AI system to a database of low-pass Gaussian filtered defocused spot images computed using equations 3 and spatially blurred using the bandwidth limit imposed by equation 6. The AI system can be trained to recognize and report values of β to monitor seeing quality as well as the desired Zernike terms.

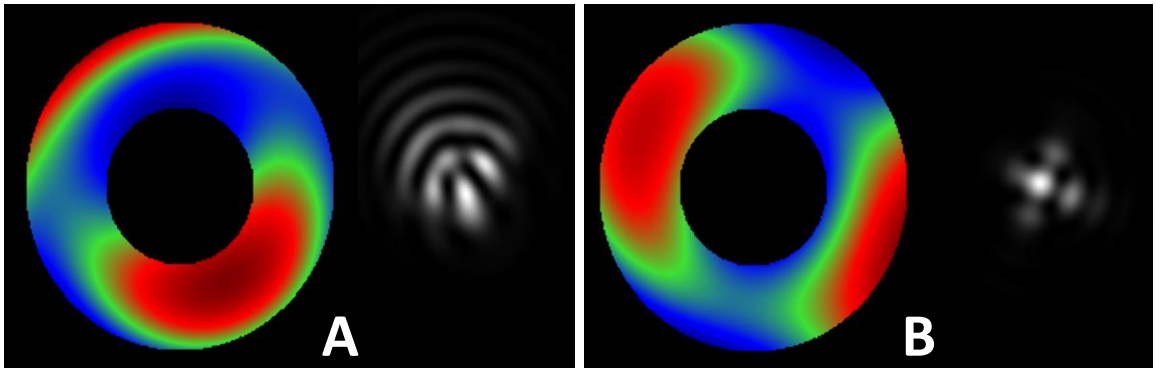

Figure 9. Alignment of a 0.6m, F/8 Ritchey Chretien telescope secondary mirror tilt using a star with a 550 nm filter. A) The pre-alignment wavefront and computed PSF with rms = 0.25wv and Strehl = 14%. Seeing reported at 1.4 arc-sec. B) Post alignment wavefront and PSF with rms = 0.14 wv and Strehl = 43%. Seeing reported at 1.5 arc-sec. Secondary offset was not adjusted and residual astigmatic errors were judged acceptable. Data provided by Cyril Cavadore from ALCOR SYSTEM. With permission of Planète Mars Observatoire Hubert Reeves - Club d'Astronomie de MARS, Saint Romain le Désert, 07320 MARS, France.

Figure 9 shows the results for aligning a 0.6m RC telescope using the AI system describe here trained for atmospheric seeing with a star as the source. As discussed above, seeing acts as a low pass filter to attenuate the fine details in the diffraction pattern of the defocused star image, however the low spatial frequencies of the irradiance pattern maybe still be sufficient to retrieve the low order Zernike terms

with enough accuracy to achieve accurate telescope alignment. An initial comparison between this AI based wavefront sensing and the data from a 100x100 Shack-Hartmann sensor for this telescope indicates a good correlation. More work is needed to better characterize its performance under different seeing conditions, but initial results look very encouraging.

Since curvature wavefront sensing has been used, with success, for adaptive optics in astronomy [3], we could expect that the AI based approach may also work on short term exposures assuming that the synthetic database is made accordingly. The speckle nature of the images is probably less of a limitation than low SNR and the reduced contrast caused by atmospheric scintillation when using a single defocus star image. Hickson and Burley [4] have shown that the scintillation noise is typically less than about 2% of the curvature signal. More investigation is needed to explore the limitations of an AI based approach in the context of adaptive optics and higher order aberration terms.

7. CONCLUSION

The results here demonstrate that the AI system can produce repeatable results that closely correlate with other wavefront sensing methods. Clearly, the ultimate accuracy is limited by the fidelity of the training data, which must account for source coherence issues. But that's ultimately an indication of the sensitivity of the method. Clearly an advantage of using AI as a wavefront sensor is that it can eliminate the need for special hardware, such as a Shack-Hartmann sensor. In many cases, where a camera already looks at a point source, the only requirement is to be able to control focus and to run special software. Another advantage is that AI can be easily configured to measure wavefront performance across the field with a single frame as shown by Baudat [7]. It is also possible to configure the AI system to recognize wavefront errors as well as obscuration ratio and atmospheric seeing parameters at multiple points across the field--and all at the same time in a single frame!

One notable limitation of the AI approach is that since it relies on a single, direct measurement of irradiance, it is very sensitive to any stray light that is unrelated to the signal. Even small amounts of stray light can cause significant errors in the output so stray light control and digital image pre-processing becomes very important with this approach.

Finally, the authors want to thank 4D Technology for making a PhaseCam available and for their assistance in making these measurements possible, Gérard Bouvet president of the Club d'Astronomie de MARS for access to their 0.6m RC telescope of Planète Mars Observatoire Hubert Reeves, as well as Cyril Cavadore from ALCOR SYSTEM for using our approach and providing the data of the alignment of their telescope.

References

[1] A. Behr, "A proposal for the alignment of large telescopes", Astron. Astrophysics. 28, 355-358 (1973).

[2] Suiter, Harold Richard, "Star Testing Astronomical Telescopes, A Manual for Optical Evaluation and Adjustment – 2nd ed.", Willmann Bell, Inc., 2013

[3] Claude Roddier and Fransois Roddier, "Wave-front reconstruction from defocused images and the testing of ground-based optical telescopes", J. Opt. Soc. Am. A/Vol. 10, No. 11 (November 1993)

[4] Paul Hickson & Greg Burley, "Single-image wavefront curvature sensing", SPIE Adaptive Optics Astronomy, vol. 2201, 549-553 (1994)

[5] Hickson, P, "Wave-front curvature sensing from a single defocused image", Vol. 11, No. 5, J. Opt. Soc. Am. A, 1667-1673 (May1994)

[6] Yohei Nishizaki and al. “Deep learning wavefront sensing”, Vol. 27, N0. 1, Optics Express, 240-250 (7 January 2019)

[7] Baudat, G., “Low-cost wavefront sensing using artificial intelligence (AI) with synthetic data”, Proc. SPIE 11354, Optical Sensing and Detection VI April 1, 2020 Strasbourg, France.

[8] Shannon, Robert R, Wyant, James C., Applied Optics and Optical Engineering, Volume 11, Academic Press, 1992, pp 28-38.

[9] Mahajan, Virendra N., Optical Imaging and Aberrations, Part II Wave Diffraction Optics, SPIE Press, 2011, p299.

[10] James Millerd, Neal Brock, John Hayes, Michael North-Morris, Matt Novak and James Wyant, “Pixelated Phase-Mask Dynamic Interferometer”, Proceedings of SPIE Vol. 5531 (SPIE, Bellingham, WA), page 304-314, 2004

[11] J. Millerd, N. Brock, J. Hayes, B. Kimbrough, M. Novak, M. North-Morris and J. C. Wyant, "Modern Approaches in Phase Measuring Metrology", Proceedings of SPIE Vol. 5856 (SPIE, Bellingham, WA), page 14-22, 2005

[12] M. Novak, J. Millerd, N. Brock, M. North-Morris, J. Hayes, and J. Wyant, "Analysis of a micropolarizer array-based simultaneous phase-shifting interferometer", APPLIED OPTICS, Vol. 44, page 6861, 10 November 2005

[13] N. Brock, J. Hayes, B. Kimbrough, J. Millerd, M. North-Morris, M. Novak and J. C. Wyant, "Dynamic Interferometry", Proceedings of SPIE Vol. 5875 (SPIE, Bellingham, WA), page 58750F-1, 2005

[14] J. Hayes, J. Millerd, " Dynamic Interferometry, Getting Rid of the Jitters", Photonics Handbook, H-34, 2006

[15] Fried, D. L. "Optical Resolution Through a Randomly Inhomogeneous Medium for Very Long and Very Short Exposures". Journal of the Optical Society of America. vol. 56, no. 10, 1372–1379 (1966).

[16] Moffat, A. F. J. “A Theoretical Investigation of Focal Stellar Images in the Photographic Emulsion and Application to Photographic Photometry”, Astronomy and Astrophysics, Vol. 3, 455 (1969).